ACS NANO

www.acsnano.org

ARTICLE

Self-Powered Circularly Polarized Light Detection Enabled by Chiral Two-Dimensional Perovskites with Mixed Chiral–Achiral Organic Cations

Xiaoyu Zhang, Yuanze Xu, Anna Niamh Alphenaar, Shripathi Ramakrishnan, Yugang Zhang, Adewale Joseph Babatunde, and Qiuming Yu*

Cite This: *ACS Nano* 2024, 18, 14605–14616

Read Online

ACCESS | Metrics & More | Article Recommendations | Supporting Information

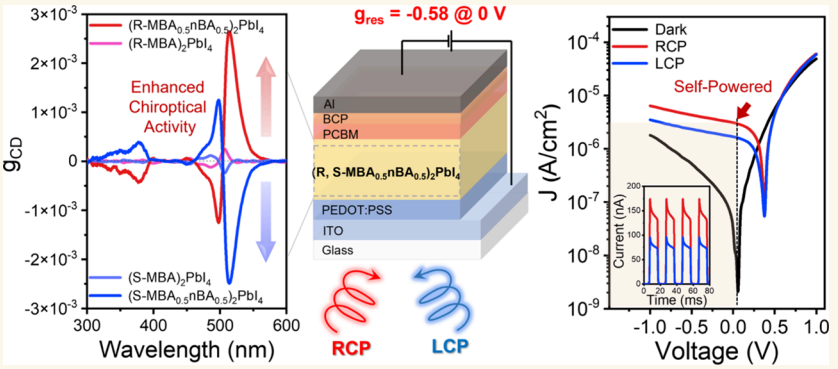

ABSTRACT: **Direct detection of circularly polarized light (CPL) holds great promise for the development of various optical technologies. Chiral 2D organic–inorganic halide perovskites make it possible to fabricate CPL-sensitive photodetectors. However, selectively detecting left-handed circularly polarized (LCP) and right-handed circularly polarized (RCP) light remains a significant challenge. Herein, we demonstrate a greatly enhanced distinguishability of photodiode-type CPL photodetectors based on chiral 2D perovskites with mixed chiral aryl (R)-(+),(S)-(−)-α-methylbenzylammonium (R,S-MBA) and achiral alkyl *n*-butylammonium (*n*BA) cations. The (R,S-$MBA_{0.5}nBA_{0.5})_2PbI_4$ perovskites exhibit a 10-fold increase in circular dichroism signals compared to (R,S-$MBA)_2PbI_4$ perovskites. The CPL photodetectors based on the mixed-cation perovskites exhibit self-powered capabilities with a specific detectivity of 2.45 × 10^{12} Jones at a 0 V bias. Notably, these devices show high distinguishability (g_{res}) factors of −0.58 and +0.54 based on (R,S-$MBA_{0.5}nBA_{0.5})_2PbI_4$ perovskites, respectively, surpassing the performance of (R-$MBA)_2PbI_4$-based devices by over 3-fold and setting a record for CPL detectors based on chiral 2D *n* = 1 perovskites.**

KEYWORDS: *circularly polarized light detection, self-powered, chiral two-dimensional perovskites, chirality, mixed cations*

INTRODUCTION

Circularly polarized light (CPL) represents an electromagnetic wave, with the electric field vector undergoing circular rotation during its propagation through space. CPL has found diverse applications, including satellite communication and 5G technologies,[1] quantum computing,[2,3] spin-optical communication,[4] drug screening,[5] information security,[6] and remote sensing.[7] To efficiently detect external CPL signals, specialized CPL-sensitive photodetectors are essential and capable of converting CPL signals into electrical ones. Due to the absence of inherent chirality in inorganic semiconductors such as Si and InGaAs, a quarter-wave plate and a linear polarizer are typically attached to conventional photodetectors for the detection of

Received: February 23, 2024
Revised: May 5, 2024
Accepted: May 13, 2024
Published: May 21, 2024

https://doi.org/10.1021/acsnano.4c02588
ACS Nano 2024, 18, 14605–14616

CPL. However, this configuration results in a significant loss of sensitivity and resolution within the light detection system, adds complexity to the design, and increases overall costs. To achieve device miniaturization, chiral-sensitive materials are employed to construct CPL-sensitive photodetectors capable of distinguishing between left-handed circularly polarized (LCP) and right-handed circularly polarized (RCP) light. In this context, chiral organic−inorganic halide perovskites have emerged as promising candidates for CPL-sensing materials due to their outstanding attributes, such as high absorption coefficients, tunable band gaps, and favorable charge-carrier mobilities.[8−11]

Chiral perovskites typically have reduced dimensional structures, such as Ruddlesden−Popper two-dimensional (2D) perovskites, in which the corner-shared metal halide octahedron inorganic frameworks are separated by large chiral organic cations.[8−11] The general formula for chiral 2D perovskites is A'_2BX_4, where A′ is a bulky chiral organic monoammonium cation, B is a divalent metal cation, and X is a halide anion. The chiroptical properties observed in chiral 2D perovskites are attributed to the chirality transfer from the A′-site chiral monoammonium cations to the achiral $[BX_6]^{4-}$ inorganic frameworks.[12,13] The NH_3^+ groups of the chiral A'-site cations penetrate into the corner shared $[BX_6]^{4-}$ inorganic frameworks, forming asymmetric hydrogen bonding with the X-site halides, which triggers the asymmetric tilting distortion of $[BX_6]^{4-}$ octahedra and ultimately results in chirality transfer. Consequently, the chiroptical phenomena observed in chiral 2D perovskites occurs at the first excitonic state of the distorted inorganic framework, which is distinct from the excitonic state of A′-site chiral organic cations.[14] Moreover, the degree of chirality transfer emerges as a critical factor in the chiroptical activity exhibited by chiral 2D perovskites.

Several chiral organic cations, such as (R)/(S)-methylbenzylammonium ((R)/(S)-MBA$^+$),[14−21] (R)/(S)-β-methylphenethylammonium ((R)/(S)-MPA$^+$),[22,23] and (R)/(S)-1−1-naphthyl-ethylammonium ((R)/(S)-1-NEA$^+$),[13,24] have been utilized as the A′-site chiral cations to demonstrate the effect of chemical structure of organic cations on chirality transfer. Additionally, the approach by mixing cations with different chemical characteristics has also been explored for augmenting the chiroptical properties of chiral 2D perovskites, attributed to the stronger asymmetry in tilting distortion of $[BX_6]^{4-}$ and the hydrogen bonding interactions.[25,26] Yan et al. demonstrated both signal inversion and a 2-fold increase in amplitude of the circular dichroism (CD) spectra by blending chiral (R)/(S)-β-methylphenethylammonium ((R)/(S)-MPA$^+$) with achiral (propylammonium or butylammonium) spacer cations in a 1:1 molar ratio. The anisotropy factors of circular dichroism (g_{CD}) at the exciton peak for pure R and S chiral systems are -1.2×10^{-4} and 1.3×10^{-4}, respectively, while the mixed-cation perovskites exhibit doubled g_{CD} values of 2.5×10^{-4} and -2.7×10^{-4}, respectively.[25] Lee et al. reported a nearly 2-fold enhancement in g_{CD} values, increasing from 5.7×10^{-4} to 1×10^{-3}, by adding 10 mol % urea into $(R\text{-}MBA)_2Pb(I_{0.7}Br_{0.3})_4$.[26] Additionally, Zhu et al. mixed (R)-MPA$^+$ with achiral ethylammonium spacer cations to form $(R\text{-}MPA_{0.5}EA_{0.5})_2PbBr_4$, yielding a g_{CD} of 2.5×10^{-3}.[27]

Propelling by the success of making chiral 2D perovskites, efforts have been devoted to developing photodetectors for direct CPL detection with different device architectures.[8−11,28] The first work of the CPL photodetector adopted a phototransistor design featuring $(R/S\text{-}MBA)_2PbI_4$ microplates and achieved a distinguishability (g_{res}) of 0.09 and a specific detectivity (D^*) of 2.2×10^{11} Jones at 518 nm with a bias of 3 V.[21] Transitioning to a photoconductor (PC) architecture by incorporating an exfoliated $(R/S\text{-}MBA)_2PbI_4$ microplate improved both the distinguishability and detectivity to a g_{res} factor of 0.23 and a D^* value of 3.06×10^{11} Jones at 520 nm with a bias of −3 V.[18] An advantage of PC-based CPL photodetectors is their self-power capability, eliminating the need for an external bias and significantly broadening their potential applications. Recently, Zhu et al. reported a self-powered PC-based CPL photodetector with $(R\text{-}MPA_{0.5}EA_{0.5})_2PbBr_4$, achieving a g_{res} factor of 0.42 at 0 V bias, marking the highest reported g_{res} of PC-based CPL photodetectors using chiral 2D perovskites.[27] Self-powered CPL photodetectors utilizing a photodiode (PD) architecture have also been explored.[26,29,30] Wang et al. reported a self-powered PD-based CPL photodetector using $(R,S\text{-}MBA)_2PbI_4$ and achieved a g_{res} factor of 0.1 at 0 V bias.[29] Recently, a self-powered PD-based CPL photodetector utilized $(R\text{-}MBA)Pb(I_{0.7}Br_{0.3})_4$ with the inclusion of 10 mol % urea as the active layer and demonstrated a g_{res} factor of 0.27 and a D^* value of 6.02×10^{12} Jones at 475 nm with 0 V bias.[26] Using $(R\text{-}MBA)_2Pb_{0.9}Sn_{0.1}I_4$ as the active layer, a g_{res} factor of 0.44 was achieved, which was the highest reported g_{res} of the PD-based CPL photodetector using chiral 2D perovskites, along with a D^* value of 1.63×10^{11} Jones at 500 nm with 0 V bias.[30] It is worth noting that the maximum g_{res} factors of −2 or +2 would be produced upon pure RCP or LCP light detection in an ideal system. Therefore, further advancements in developing CPL photodetectors rely on the enhancement of the chirality of chiral 2D perovskites to increase the distinguishable generation of electron−hole pairs upon RCP/LCP light illumination and the careful design of photodiode architectures to efficiently separate, transfer, and collect RCP/LCP photogenerated charges within the devices.

In this work, we develop photodiode-type CPL detectors based on chiral 2D perovskites with mixing chiral aryl cations ((R)-(+),(S)-(−)-α-methylbenzylammonium, (R)/(S)-MBA$^+$) and achiral alkyl cations (n-butylammonium, nBA$^+$) in the organic layer and demonstrate a high distinguishability. nBA$^+$ is selected because it has a similar molecular length as R,S-MBA$^+$, which could lead to a similar penetration into the inorganic framework to form hydrogen bonding and, meanwhile, to reduce the van der Waals gap between two organic layers. Additionally, nBA$^+$ lacks π-conjugation, making the alkyl tail flexible to interact with aryl R,S-MBA$^+$, which could lead to "maximizing" the influence on hydrogen bonding and, thus, chirality transfer. The optimized morphology and thickness of chiral 2D $(R,S\text{-}MBA_{0.5}nBA_{0.5})_2PbI_4$ perovskite thin films result in a significantly enhanced g_{CD} of 2.89×10^{-3}, which is a 10-fold enhancement in chirality amplitude compared to $(R,S\text{-}MBA)_2PbI_4$ containing pure chiral aryl cations. The enhanced chirality of $(R,S\text{-}MBA_{0.5}nBA_{0.5})_2PbI_4$ perovskites can increase the distinguishable generation of electron−hole pairs upon RCP/LCP light illumination. Furthermore, the $(R\text{-}MBA_{0.5}nBA_{0.5})_2PbI_4$ perovskite films exhibit a preferred crystallographic orientation, facilitating charge carrier transport within the perovskite films. To effectively transport and collect charge carriers generated by RCP/LCP light and reduce dark current, we design the p-i-n-structured photodiode-type detectors with the hole and electron transport layers as well as the electrodes to have the energy levels aligned well with those of the active layer. The designed CPL detectors with the

https://doi.org/10.1021/acsnano.4c02588
ACS Nano 2024, 18, 14605−14616

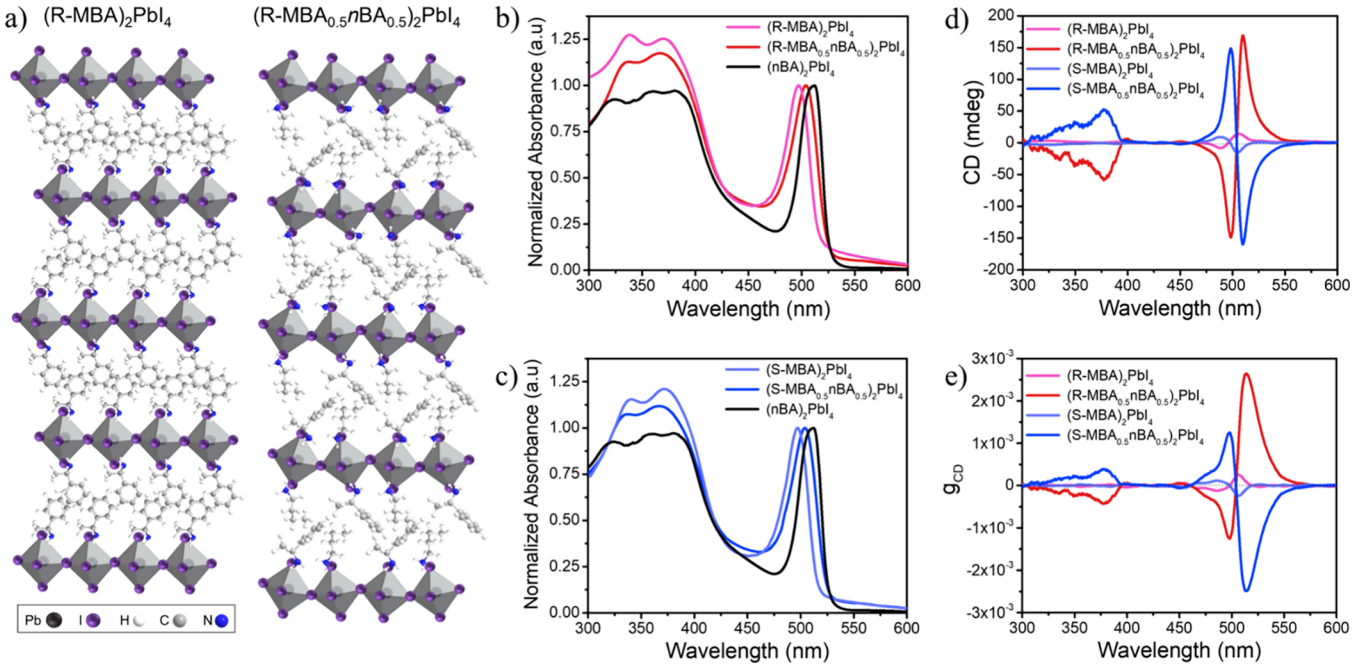

Figure 1. (a) Schematics of the crystal structures of $(R\text{-}MBA)_2PbI_4$ and $(R\text{-}MBA_{0.5}nBA_{0.5})_2PbI_4$. (b, c) Normalized UV−vis absorption spectra, (d) circular dichroism (CD) spectra, and (e) calculated anisotropy factor (g_{CD}) of the 0.3 M $(R,S\text{-}MBA)_2PbI_4$, $(R,S\text{-}MBA_{0.5}nBA_{0.5})_2PbI_4$, and $(nBA)_2PbI_4$ thin films.

optimal active layer thickness of $(R,S\text{-}MBA_{0.5}nBA_{0.5})_2PbI_4$ display self-powered capability with a specific detectivity D^* of 2.45×10^{12} Jones at 0 V bias. Moreover, these CPL detectors exhibit high g_{res} factors of −0.58 and +0.54 at 0 V bias, respectively, surpassing the value for devices based on $(R,S\text{-}MBA)_2PbI_4$ by over 3-fold. Notably, this value surpasses the reported highest g_{res} factors of the CPL detectors based on chiral 2D perovskites.

RESULTS AND DISCUSSION

We made chiral 2D perovskite thin films via a one-step solution process. To manipulate the chirality, we blended chiral organic cations R-MBA^+ and S-MBA^+ with achiral cations nBA^+ to form the organic spacers composed of pure chiral aryl cations, mixed chiral aryl and achiral alkyl cations, and pure achiral alkyl cations. Using precursor solutions with a concentration of 0.3 M for Pb^{2+} and varied amounts of chiral/achiral ammonium halide salts, we obtained thin films of chiral 2D perovskites $(R,S\text{-}MBA)_2PbI_4$ and $(R,S\text{-}MBA_{0.5}nBA_{0.5})_2PbI_4$ and achiral 2D perovskite $(nBA)_2PbI_4$. The schematic diagrams of the crystal structures of $(R\text{-}MBA)_2PbI_4$ and $(R\text{-}MBA_{0.5}nBA_{0.5})_2PbI_4$ are shown in Figure 1a. The linear optical properties of the films are investigated through UV−vis absorption spectroscopy. As shown in Figure 1b,c, all 2D perovskite films exhibit typical features of a lower-energy exciton peak due to strong dielectric confinement in $n = 1$ 2D perovskites and a high-energy continuum absorption edge with two humps, corresponding to the transitions in the inorganic frameworks.[31] The exciton peak was observed at 497 nm for $(R,S\text{-}MBA)_2PbI_4$ and redshifted to 504 nm for $(R,S\text{-}MBA_{0.5}nBA_{0.5})_2PbI_4$ and further to 513 nm when all the (R)/(S)-MBA^+ cations were substituted with nBA^+ cations. This redshift aligns with the results of chiral 2D perovskites with mixed alkyl−aryl cations,[25] which could be either due to a reduced band gap or increased exciton binding energy induced by the inclusion of nBA^+ cations in the chiral 2D perovskites. In contrast, the two humps in the high-energy continuum absorption range were blueshifted from 338 and 370 nm for $(R,S\text{-}MBA)_2PbI_4$ to 335 and 366 nm for $(R,S\text{-}MBA_{0.5}nBA_{0.5})_2PbI_4$. Density function theory (DFT) calculations show that the valence band maximum (VBM) is formed by the antibonding between the s orbital of metal (B) and the p orbital of halide (X) and the conduction band minimum (CBM) is composed by the nonbonding between the p orbital of metal and the p orbital of halide.[32,33] Therefore, any change in B−X bond length or X−B−X bond angle can lead to the shift of energy level of VBM and CBM and, thus, the band gap. The absorption peak shifts observed in the $(R,S\text{-}MBA_{0.5}nBA_{0.5})_2PbI_4$ films compared to the $(R,S\text{-}MBA)_2PbI_4$ films indicate that the X−B−X (here I−Pb−I) bond angles could have changed due to the octahedral tilting induced by mixed cations. The photoluminescence (PL) spectra show exciton emission behavior (Figure S1a). The excitonic PL peak of the $(R\text{-}MBA_{0.5}nBA_{0.5})_2PbI_4$ perovskites positioned between those of pure chiral $(R\text{-}MBA)_2PbI_4$ and achiral $(nBA)_2PbI_4$ perovskites, which is consistent with the absorption spectral trend.

We further investigated the chiroptical activity of our chiral 2D perovskites by circular dichroism (CD) spectroscopy. As shown in Figure 1d, all chiral 2D perovskites exhibit CD signals in the range between 450 and 550 nm, while the CD signals are in the range between 220 and 300 nm for the R,S-MBAI thin films (Figure S1b), confirming the transfer of chirality from the chiral organic cations to the $[PbI_6]^{4-}$ inorganic frameworks. Additionally, the CD spectra of the chiral perovskite films exhibit characteristic zero-crossing features at wavelengths corresponding to their exciton peaks, which is known as the Cotton effect. This phenomenon originates from the exciton resonance splitting in the excited states induced by the presence of chiral cations.[34] The CD signal of $(S\text{-}MBA_{0.5}nBA_{0.5})_2PbI_4$ and $(S\text{-}MBA)_2PbI_4$ perovskites shows distinct opposite polarity compared to (R-

https://doi.org/10.1021/acsnano.4c02588
ACS Nano 2024, 18, 14605−14616

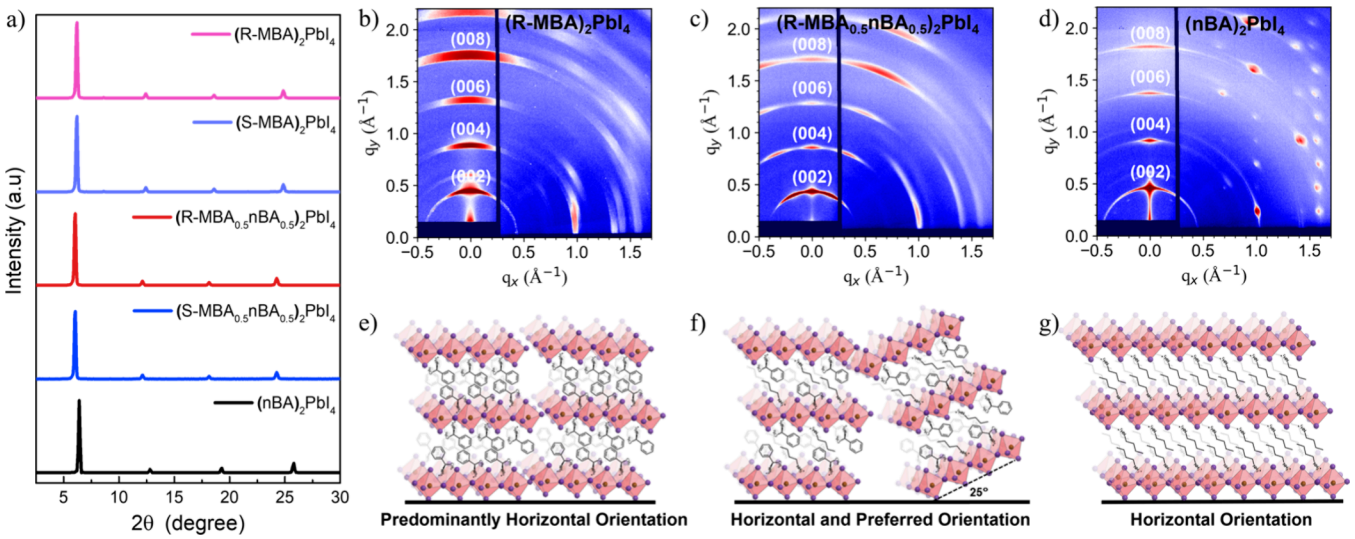

Figure 2. (a) X-ray diffraction (XRD) patterns of the 0.3 M (R,S-MBA)$_2$PbI$_4$, (R,S-MBA$_{0.5}$*n*BA$_{0.5}$)$_2$PbI$_4$, and (*n*BA)$_2$PbI$_4$ thin films. (b−d) GIWAXS patterns with the incident angle of 0.2° and (e−g) schematic illustrations of crystalline orientation of the 0.3 M (R-MBA)$_2$PbI$_4$, (R-MBA$_{0.5}$*n*BA$_{0.5}$)$_2$PbI$_4$, and (*n*BA)$_2$PbI$_4$ thin films.

MBA$_{0.5}$*n*BA$_{0.5}$)$_2$PbI$_4$ and (R-MBA)$_2$PbI$_4$, corresponding to the opposite handedness of the chiral ligand used. Moreover, (R,S-MBA$_{0.5}$*n*BA$_{0.5}$)$_2$PbI$_4$ perovskites show a significantly enhanced CD signal (~±170 mdeg), with a magnitude about 10 times greater than that of (R,S-MBA)$_2$PbI$_4$. Additionally, the CD signals were unchanged when the measurements were conducted from the front and back sides of the chiral 2D perovskites thin films (Figure S1c,d), indicating the absence of the antisymmetric linear dichroism and linear birefringence (LDLB) effect that originates from macroscopic anisotropy.[35−37] This confirmed that the notable enhancement in chiroptical responses of (R,S-MBA$_{0.5}$*n*BA$_{0.5}$)$_2$PbI$_4$ is attributable to the influence of the mixed aryl, chiral and alkyl, achiral cations rather than the antisymmetric LDLB contribution.[35−37]

To further quantify the impact of mixing chiral and achiral cations on the chiroptical activity of chiral 2D perovskites, the anisotropy factor (g_{CD}) was calculated with the following equation:[38]

$$g_{CD} = \frac{\mathrm{CD[mdeg]}}{32{,}980 \times \mathrm{absorbance}} = \frac{\Delta A}{A} \quad (1)$$

where ΔA is the difference between the absorbance of left-handed (A_L) and right-handed (A_R) CPL. As shown in Figure 1e, the g_{CD} values of (R,S-MBA)$_2$PbI$_4$ were calculated to be 2.48×10^{-4} and -2.37×10^{-4}, respectively. In contrast, the (R,S-MBA$_{0.5}$*n*BA$_{0.5}$)$_2$PbI$_4$ films show 1 order of magnitude higher g_{CD} values of 2.64×10^{-3} and -2.49×10^{-3}, respectively, which are comparable to those reported 2D chiral perovskites.[20,24−27,30] This significant g_{CD} enhancement further demonstrates that the incorporation of achiral *n*BA$^+$ cations in chiral 2D perovskites amplifies their chiroptical properties.

We then confirmed that all perovskites adopt a layered structure with chiral/achiral cations located between $[PbI_6]^{4-}$ frameworks by X-ray diffraction (XRD) analysis. As shown in Figure 2a, all of the samples show sharp periodicity diffraction peaks, implying that the chiral 2D perovskites preferentially grow parallel to the (002 l) planes. Specifically, the XRD pattern of chiral (R,S-MBA)$_2$PbI$_4$ exhibits diffraction peaks at 6.19°, 12.38°, 18.58°, and 24.82°, corresponding to the (002), (004), (006), and (008) planes of 2D perovskites, respectively, with an interlayer spacing ($d_{(002)}$) of 14.26 Å. The achiral (*n*BA)$_2$PbI$_4$ exhibits diffraction peaks at 6.4°, 12.8°, 18.98°, and 25.76°, assigned to the (002), (004), (006), and (008) planes, respectively, corresponding to a $d_{(002)}$ of 13.79 Å. In contrast, (R,S-MBA$_{0.5}$*n*BA$_{0.5}$)$_2$PbI$_4$ displays the (002) diffraction peak at 6.05°, indicating an expanded $d_{(002)}$ of 14.7 Å, followed by the (004) peak at 12.1°, the (006) peak at 18.16°, and the (008) peak at 24.27°. This expansion in interlayer distance can be attributed to the packing conformational differences of the phenyl ring moiety due to the insertion of alkyl cations.[25] As shown in Figure 1a, the packing conformation could change along the out-of-plane direction by mixing alkyl-aryl cations. This leads to asymmetric hydrogen bonding between NH_3^+ on the alkyl and aryl monoammonium cations and I^- on the equatorial and axial position of octahedra and enhances asymmetric distortion of the inorganic framework, thereby amplifying the chirality.

To further elucidate the crystalline orientation of the chiral and achiral 2D perovskites, we conducted grazing-incidence wide-angle X-ray scattering (GIWAXS) measurements with an incident angle of 0.20°. As shown in Figures 2b−d, the *q* values of the (002 l) Debye−Scherrer rings and Bragg spots agree well with the XRD results where *q* is the scattering vector for the diffraction features. Specifically, the (R-MBA)$_2$PbI$_4$ and (*n*BA)$_2$PbI$_4$ films (Figure 2b,d) exhibit strong diffraction signals for (002 l) planes predominantly in the out-of-plane direction, while the (R-MBA$_{0.5}$*n*BA$_{0.5}$)$_2$PbI$_4$ film exhibits segments on the Debye−Scherrer rings for (002 l) planes with the preferred crystallographic orientation (Figure 2c). The azimuthal GIWAXS patterns and the azimuth angular distribution of the (002) planes of all perovskites are shown in Figure S2a−c,d, respectively. Due to rotational isotropy around the substrate normal, the scattering is symmetric in the azimuthal angle. The distribution from 0° to 90° provides comprehensive information about the orientation distributions, while patterns between 90° and 180° indicate symmetric diffractions.[39] As shown in Figure S2d, the azimuth angular distributions of the (002) planes of both (R-MBA)$_2$PbI$_4$ and (*n*BA)$_2$PbI$_4$ reveal peak positions at 90°, confirming that the

https://doi.org/10.1021/acsnano.4c02588
ACS Nano 2024, 18, 14605−14616

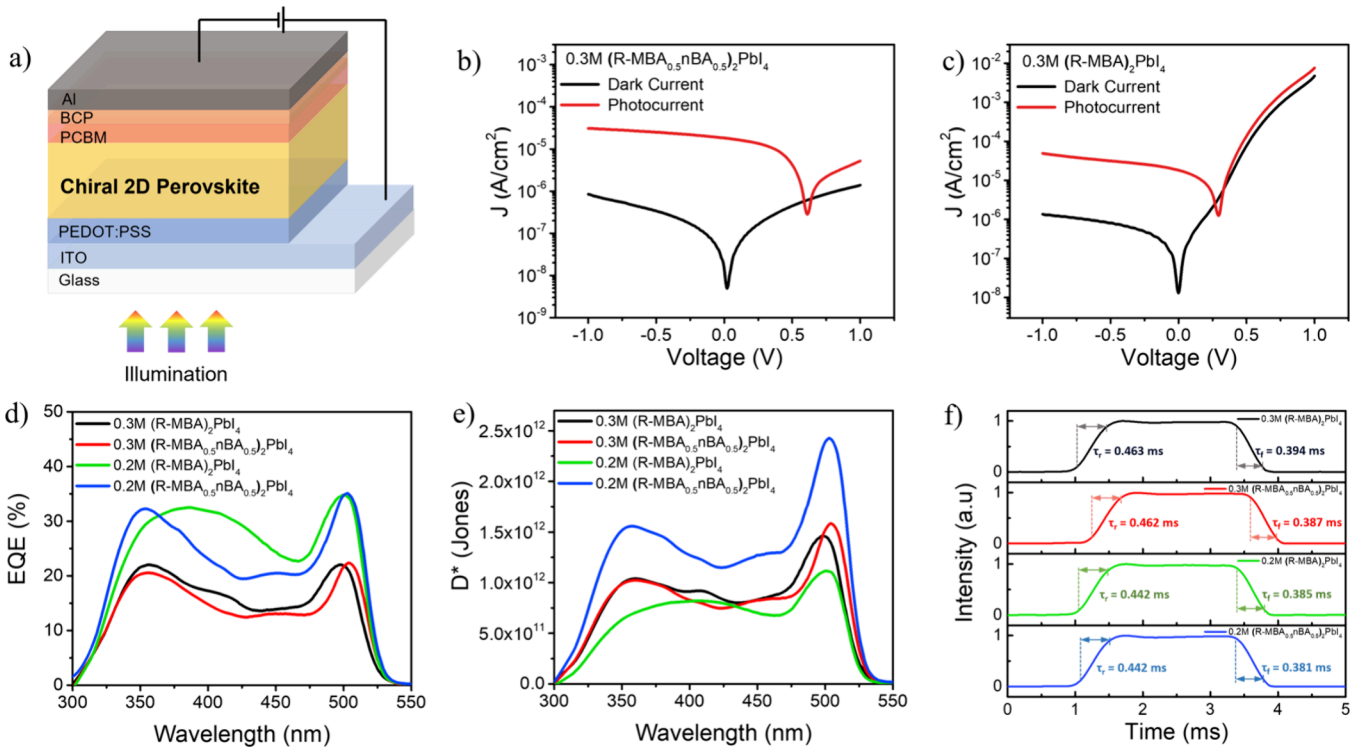

Figure 3. (a) Schematic diagram of a chiral perovskite-based photodetector. (b, c) $J-V$ curves of the photodetectors with the 0.3 M (R-$MBA_{0.5}nBA_{0.5})_2PbI_4$ and (R-$MBA)_2PbI_4$ films, respectively, measured in the dark and under monochromatic unpolarized light illumination at 500 nm and 1.0 mW cm^{-2}. (d) EQE, (e) specific detectivity D^*, and (f) response speed of the photodetectors with the 0.2 and 0.3 M (R-$MBA_{0.5}nBA_{0.5})_2PbI_4$ and (R-$MBA)_2PbI_4$ films under 0 V bias.

layer structures of the (R-$MBA)_2PbI_4$ and ($nBA)_2PbI_4$ films are horizontally orientated to the substrates as schematically illustrated in Figure 2e,g, respectively. The full width at half-maximum (fwhm) values of the azimuth angular distributions are 32.1° and 12.2° for the (002) planes of (R-$MBA)_2PbI_4$ and ($nBA)_2PbI_4$, respectively. This reduced fwhm of ($nBA)_2PbI_4$ indicates a decrease in the misorientation of the (002 l) crystallites, suggesting highly crystalline structure features. Notably, we observed two preferred orientations represented by three strong peaks in the orientation distribution of the (002) plane of (R-$MBA_{0.5}nBA_{0.5})_2PbI_4$ (Figure S2d). One is located at an azimuthal angle of 90°, and the other two are around 65° and 115°. These stacking patterns indicate that (R-$MBA_{0.5}nBA_{0.5})_2PbI_4$ exhibits two dominant orientations—one parallel to the substrate and the other with 2D inorganic frameworks lying against the substrate at 25°, as illustrated in Figure 2f. The impacts of the crystalline orientation on the surface morphologies of these films can be clearly observed in the scanning electron microscopy (SEM) images (Figure S3). The possible mechanism guiding this favored crystal stacking involves the manipulation of the crystal stacking orientation using mixed alkyl-aryl cations, particularly with the highly crystalline characteristics observed in ($nBA)_2PbI_4$. This manipulation reveals different crystal orientations in term of microstructural arrangements, contributing to the observed preferred crystallographic orientation.[40] This preferred orientation is considered to regulate the charge transportation in the perovskite films, potentially leading to enhancements in the performance of corresponding optoelectronics,[40] as discussed later.

For a CPL photodetector, an optimal chiral perovskite layer thickness is essential for efficient CPL photodetection. The relationship between chiral perovskite thickness and its ability to distinguish between LCP and RCP light is described by the following equation:[41]

$$\frac{\Delta c}{c} = \frac{2(c_L - c_R)}{c_L + c_R} \approx \frac{\Delta\alpha d}{\exp(\alpha_L d) - 1} \quad (2)$$

where Δc is the difference between the carrier concentration generated by LCP and RCP light illumination ($\Delta c = c_L - c_R$), c is the average carrier concentration ($c = (c_L + c_R)/2$), $\Delta\alpha$ is the difference between the absorption coefficients for LCP (α_L) and RCP (α_R) light, and d is the thickness of the chiral medium. It is important to note that the distinguishability of LCP and RCP of a photodetector, g_{res}, is equal to $\Delta c/c$ only when the conversion and collection efficiency of absorbed photons to electron−hole pairs are the same. Accordingly, increasing the thickness of the chiral perovskite leads to a decrease in the CPL response.[41] Therefore, we varied the thickness of the chiral perovskite films to investigate the film thickness effect on the distinguishability between the LCP and RCP for photodetectors.

Chiral (R-$MBA)_2PbI_4$ and (R-$MBA_{0.5}nBA_{0.5})_2PbI_4$ perovskites were fabricated via a one-step solution process with precursor concentrations of 0.2 and 0.3 M Pb^{2+} under the same conditions and achieved the film thicknesses of ∼220 and ∼330 nm, respectively (Table S1). Both the 0.2 M (R-$MBA)_2PbI_4$ and (R-$MBA_{0.5}nBA_{0.5})_2PbI_4$ films show lower absorbance and CD signal compared to the 0.3 M counterparts because of the reduced film thickness while maintaining the same exciton peak and CD signal positions (Figure S4a,b). Impressively, the 0.2 M (R-$MBA_{0.5}nBA_{0.5})_2PbI_4$ films show a g_{CD} value of 2.89×10^{-3}, surpassing the g_{CD} values of the 0.3 M (R-$MBA_{0.5}nBA_{0.5})_2PbI_4$ film (2.64×10^{-3}) and the 0.2 and 0.3

https://doi.org/10.1021/acsnano.4c02588
ACS Nano 2024, 18, 14605−14616

M (R-MBA)$_2$PbI$_4$ films (1.40−2.48 × 10^{-4}) (Figure S4c). This g_{CD} enhancement further demonstrates that introducing achiral nBA$^+$ cations in the chiral 2D perovskites amplifies the chiroptical properties, even in thinner films. Additionally, this slightly larger g_{CD} of the thinner film than that of the thicker film suggests that the symmetric LDLB interaction is minimal in the (R-MBA$_{0.5}$$nBA_{0.5}$)$_2PbI_4$ films.[35,36] (More discussion is given in Figure S1 in the Supporting Information.) We confirmed by XRD (Figure S 4d) that the 0.2 M (R-MBA)$_2$PbI$_4$ and (R-MBA$_{0.5}$$nBA_{0.5}$)$_2PbI_4$ perovskites exhibit identical (002 l) periodicity diffraction peaks as the 0.3 M counterparts, indicating that the interlayer spacing remains unchanged. The crystalline orientations were also investigated through GIWAXS measurements with an incident angle of 0.20° (Figure S5a−g). Like their counterparts of the thicker films, both the 0.2 M (R-MBA)$_2$PbI$_4$ and (nBA)$_2$PbI$_4$ films have 2D crystalline domains with the inorganic frameworks oriented in parallel to the substrate. The 0.2 M (R-MBA$_{0.5}$$nBA_{0.5}$)$_2PbI_4$ film has the 2D crystalline domains with the inorganic frameworks orientated either in parallel or 25° to the substrate but with less amount of the tilt-orientated domains as seen in the lower intensity at 65°/115° for the azimuth angular distribution of the (002) planes, as illustrated schematically in Figure S5h, owing to its lower thickness.

To realize direct CPL detection, we fabricated photodiode-type photodetectors based on chiral perovskites (R,S-MBA$_{0.5}$$nBA_{0.5}$)$_2PbI_4$ and (R,S-MBA)$_2$PbI$_4$. The chiral 2D perovskite layer is sandwiched between a transparent indium tin oxide (ITO) anode and an Al cathode, where poly(3,4-ethylenedioxythiophene)-poly(styrenesulfonate) (PEDOT:PSS) serves as the hole-transport layer (HTL), [6,6]-phenyl-C61-butyric acid methyl ester (PCBM) is the electron-transport layer (ETL), and bathocuproine (BCP) works as the hole-blocking layer (EBL), for a full device structure of ITO/PEDOT:PSS/chiral 2D perovskites/PCBM/BCP/Al (Figure 3a). The energy diagram for each layer in the fabricated devices is shown in Figure S6a. The highest occupied molecular orbital (HOMO, −6.7 eV) and lowest unoccupied molecular orbital (LUMO, −2.5 eV) levels of R-MBA were determined by cyclic voltammetry (Figure S7). Taking the values of −3.3 and −5.7 eV of the conduction band minimum (CBM) and valence band maximum (VBM), respectively, of the [PbI$_6$]$^{4-}$ inorganic layers,[42,43] (R,S-MBA)$_2$PbI$_4$ chiral 2D perovskites have a type I band alignment. The type I band alignment would be retained for (R,S-MBA$_{0.5}$$nBA_{0.5}$)$_2PbI_4$ because of the even larger band gap of the organic layer due to the insulating nature of nBA. Such device design ensures low dark current J_D, high photocurrent, and diode-rectifying behavior as shown in Figure S6b−e for the device working mechanism.

We first evaluated the performance of the chiral photodetectors under unpolarized light illumination to identify the optimal devices and to ensure no performance difference based on R- or S-chiral 2D perovskites. The current density−voltage (J−V) characteristics of the chiral photodetectors with different film thicknesses of (R-MBA$_{0.5}$$nBA_{0.5}$)$_2PbI_4$ and (R-MBA)$_2$PbI$_4$ in the dark and under monochromatic unpolarized light illumination are shown in Figure 3b,c and Figure S8a,b. The chiral photodetectors with 0.2 and 0.3 M (R-MBA$_{0.5}$$nBA_{0.5}$)$_2PbI_4$ films show the dark current J_D values of 1.78 × 10^{-6} and 8.21 × 10^{-7} A cm^{-2} at −1 V bias, respectively, while those with 0.2 and 0.3 M (R-MBA)$_2$PbI$_4$ films show the J_D of 1.06 × 10^{-5} and 1.36 × 10^{-6} A cm^{-2}, respectively. The lower J_D exhibited by the thicker film photodetectors is attributed to the lower electric field under the same bias and increased diffusion distance due to the thicker active layer. Considering that alkyl cation-based perovskites typically display stronger exciton−phonon coupling and lower exciton diffusivity in comparison to aryl cation-based perovskites,[44] the lower J_D values exhibited by the photodetectors with (R-MBA$_{0.5}$$nBA_{0.5}$)$_2PbI_4$ can be attributed to the presence of the nBA$^+$ spacer, which impedes the exciton diffusivity, resulting in the lower J_D of the devices. On the other hand, the photocurrent density (J_P) is around 1 order of magnitude larger than the J_D at −1 V bias for both (R-MBA$_{0.5}$nBA$_{0.5}$)$_2$PbI$_4$ and (R-MBA)$_2$PbI$_4$ photodetectors. Moreover, the asymmetrical electrode configuration of the photodiodes generates a built-in potential that allows the photodiodes to function even without an external bias voltage, resulting in a self-powered condition. Specifically, the photodetectors based on 0.2 and 0.3 M (R-MBA$_{0.5}$$nBA_{0.5}$)$_2PbI_4$ exhibit stronger built-in potentials of 0.65 and 0.61 V, respectively, in comparison to 0.36 and 0.29 V of the counterparts based on 0.2 and 0.3 M (R-MBA)$_2$PbI$_4$. This enhanced built-in electric field can be attributed to the presence of the nBA$^+$ spacer that induces slightly unbalanced carrier mobilities and trap densities, which will be discussed below. The higher built-in potential can effectively promote the separation and extraction of the photogenerated electron−hole pairs under illumination.[45]

We then conducted the space charge-limited current (SCLC) analysis to gain the charge carrier mobility and trap state density of 0.2 and 0.3 M (R-MBA$_{0.5}$$nBA_{0.5}$)$_2PbI_4$ and (R-MBA)$_2$PbI$_4$ films using the fabricated electron-only and hole-only devices with the configuration of ITO/SnO$_2$/chiral 2D perovskites/PCBM/Ag and ITO/PEDOT:PSS/chiral 2D perovskites/MoO$_3$/Ag, respectively (Figure S9).[46] The dark J−V characteristics of the electron-only and hole-only devices display three regions: an ohmic region at low bias with a linear relationship between the current and the electric field, a trap-filled limited region at intermediate bias showing a sharp increase in current, and a trap-free space charge-limited-current (SCLC) region at high bias.[47] In the trap-filled limited region, trap density levels are progressively filled, reaching full saturation at the trap-filled limit voltage (V_{TFL}). The carrier trap density and charge carrier mobility, N_{trap} and μ, can be calculated using the following equation:[48]

$$N_{trap} = \frac{2\varepsilon_r\varepsilon_0 V_{TFL}}{qL^2} \tag{3}$$

$$J_D = \frac{9\varepsilon_r\varepsilon_0\mu V_{TFL}^2}{8L^3} \tag{4}$$

where ε_r is the relative permittivity of perovskites (∼4),[49] ε_0 is the vacuum permittivity (8.8 × 10^{-12} F m^{-1}), q is the elemental charge, L is the thickness of the chiral 2D perovskites, V_{TFL} is the trap-filled limit voltage, and J_D is the dark current density at V_{TFL}. The results are summarized in Table S2 and plotted in Figure S10. With comparable thickness, (R-MBA$_{0.5}$$nBA_{0.5}$)$_2PbI_4$ films show higher $N_{trap,e/h}$ and lower $\mu_{e/h}$ than (R-MBA)$_2$PbI$_4$ films. Due to the decreased diffusion distance of the thinner films, the thinner films of both (R-MBA$_{0.5}$$nBA_{0.5}$)$_2PbI_4$ and (R-MBA)$_2$PbI$_4$ exhibit lower $N_{trap,e/h}$ and higher $\mu_{e/h}$ in comparison to their thicker counterparts. The differences in $N_{trap,e/h}$ and $\mu_{e/h}$ between the 0.2 and 0.3 M (R-MBA$_{0.5}$$nBA_{0.5}$)$_2PbI_4$ films are not as

https://doi.org/10.1021/acsnano.4c02588
ACS Nano 2024, 18, 14605−14616

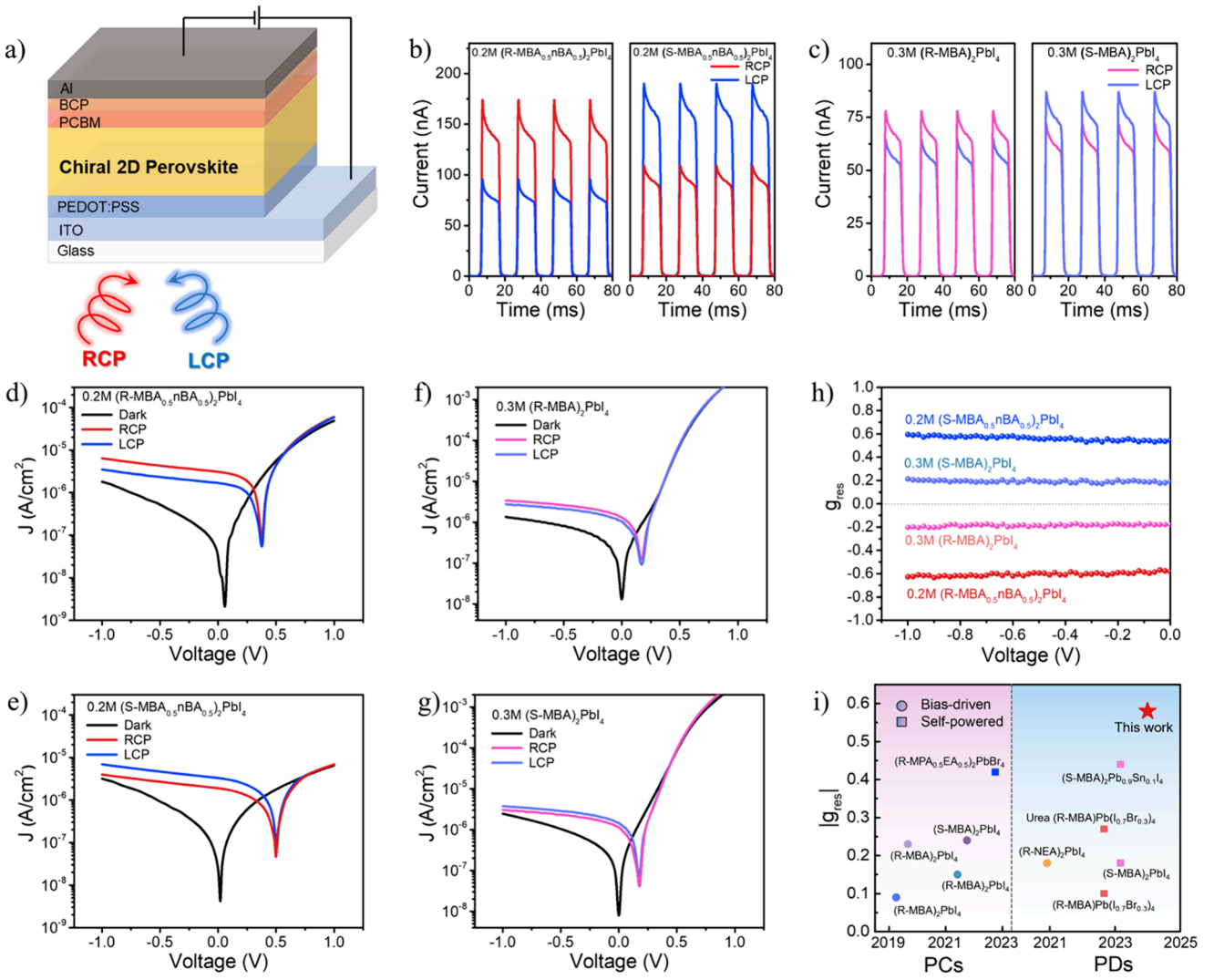

Figure 4. (a) Schematic illustration of RCP and LCP light detection of the chiral 2D perovskite-based photodetectors. (b, c) Photocurrent density-dependent time ($J-T$ curves) at 0 V bias and (d–g) $J-V$ curves of the photodetectors with the 0.2 M (R,S-MBA$_{0.5}$$nBA_{0.5}$)$_2PbI_4$ and 0.3 M (R,S-MBA)$_2$PbI$_4$ films measured in the dark and under monochromatic RCP and LCP light illumination of 0.5 mW cm^{-2} at 510 and 505 nm, respectively. (f) Calculated distinguishability (g_{res}) of 0.2 M (R,S-MBA$_{0.5}$$nBA_{0.5}$)$_2PbI_4$ and 0.3 M (R,S-MBA)$_2$PbI$_4$ devices over the bias range of −1.0 to 0 V. (i) Summary of g_{res} asymmetry factors of some reported CPL detectors based on 2D chiral perovskites.

significant as the counterparts of (R-MBA)$_2$PbI$_4$. This phenomenon can be contributed to the higher degree of preferred orientation in the 0.3 M (R-MBA$_{0.5}$$nBA_{0.5}$)$_2PbI_4$ perovskite (Figure 2f and Figure S5h), resulting in the relatively enhanced out-of-plane charge transport ability. These carrier mobilities and trap densities explain the trend of dark current densities observed in the photodetectors. We also notice a slightly increased unbalanced hole and electron mobilities ($\mu_h > \mu_e$) and trap densities ($N_{trap,h} < N_{trap,e}$) of (R-MBA$_{0.5}$$nBA_{0.5}$)$_2PbI_4$ films. Therefore, the photogenerated electrons in (R-MBA$_{0.5}$$nBA_{0.5}$)$_2PbI_4$ have a greater tendency to be trapped and accumulated close to their interface with transporting layers. Under forward bias, the electron trapping at the (R-MBA$_{0.5}$$nBA_{0.5}$)$_2PbI_4$/PEDOT:PSS interface induces band bending of (R-MBA$_{0.5}$$nBA_{0.5}$)$_2PbI_4$, thus reducing the Schottky junction thickness and facilitating the hole injection, which lead to larger built-in potentials upon illumination compared to devices based on (R-MBA)$_2$PbI$_4$. Moreover, the unbalanced hole and electron mobilities and trap densities diminish for the thicker films, which could lead to the reduced built-in potentials observed in the photodetectors with thicker 2D chiral perovskite films.

The external quantum efficiency (EQE) of the devices is defined as the ratio of charge carriers collected to incident photons. As the self-powered chiral photodetectors, the EQE spectra were measured under unpolarized illumination with different wavelengths of light at a 0 V bias, as shown in Figure 3d. Corresponding to the absorption of (R,S-MBA$_{0.5}$$nBA_{0.5}$)$_2PbI_4$ and (R,S-MBA)$_2$PbI$_4$ perovskites, all devices show an EQE response from 300 to 550 nm. Comparable EQE peak values are shown for the photodetectors based on (R-MBA$_{0.5}$$nBA_{0.5}$)$_2PbI_4$ and (R-MBA)$_2$PbI$_4$ with similar thicknesses at 503 and 498 nm, respectively, which correspond to their exciton peaks. For the wavelength below 500 nm, the (R-MBA$_{0.5}$$nBA_{0.5}$)$_2PbI_4$ photodetectors consistently exhibit lower EQE values compared to the (R-MBA)$_2$PbI$_4$ counterparts with similar thicknesses. This difference is attributed to the lower electron and hole mobilities in the (R-MBA$_{0.5}$$nBA_{0.5}$)$_2PbI_4$ films (Table S2). Additionally, the photodetectors with thinner 2D chiral perovskite films show

https://doi.org/10.1021/acsnano.4c02588
ACS Nano 2024, 18, 14605−14616

Table 1. Summary of Representative CPL Photodetectors Based on Chiral 2D Perovskites

device type	chiral 2D perovskite	CD (mdeg)	g_{CD}	D^* (Jones)	$\lvert g_{res}\rvert$	ref.
PCs (photoconductors)	$(R\text{-}MBA)_2PbI_4$	~50	-	3.06×10^{11}	0.23	18
	$(R\text{-}MBA)_2PbI_4$	~20	-	1.15×10^{13}	0.15	19
	$(S\text{-}MBA)_2PbI_4$	~10	3×10^{-4}	3.9×10^{12}	0.24	20
	$(R\text{-}MBA)_2PbI_4$	~130	-	2.2×10^{11}	0.09	21
	$(R\text{-}MPA_{0.5}EA_{0.5})_2PbBr_4$	~30	2.5×10^{-3}	-	0.42	27
PDs (photodiodes)	$(R\text{-}NEA)_2PbI_4$	~50	3×10^{-3}	-	0.18	24
	$(R\text{-}MBA)Pb(I_{0.7}Br_{0.3})_4$	~12	4×10^{-4}	6.10×10^{12}	0.1	26
	urea $(R\text{-}MBA)Pb(I_{0.7}Br_{0.3})_4$	~30	8×10^{-4}	6.02×10^{12}	0.27	26
	$(S\text{-}MBA)_2PbI_4$	~160	1.8×10^{-3}	-	0.18	30
	$(S\text{-}MBA)_2Pb_{0.9}Sn_{0.1}I_4$	~150	1.6×10^{-3}	1.63×10^{11}	0.44	30
	$(R\text{-}MBA_{0.5}nBA_{0.5})_2PbI_4$	~170	2.9×10^{-3}	2.45×10^{12}	0.58	This work

significantly higher EQE values (~35.3% at 503 nm) than those (~22.6% at 498 nm) of the counterparts with thicker films. Despite the lower light absorption efficiency of thinner chiral 2D perovskite films, their lower $N_{trap,e/h}$, higher $\mu_{e/h}$, and higher internal electric field collectively enhance the charge transport and facilitate the extraction of carriers from energy barriers, leading to higher EQEs.

The chiral photodetectors were also evaluated in terms of their responsivity R and specific detectivity D^*. The responsivity R in the unit of A/W, which is defined as the ratio of photocurrent to intensity of incident light, can be calculated from the EQE according to eq 5:

$$R = \frac{\mathrm{EQE}\cdot e}{h\nu} \tag{5}$$

where h is the Plank constant, ν is the photon frequency, and e is the elementary charge. Figure S11a shows that the 0.2 and 0.3 M $(R\text{-}MBA_{0.5}nBA_{0.5})_2PbI_4$ photodetectors exhibit the R values with maxima of 0.142 and 0.091 A/W at 503 nm under 0 V bias, respectively, overperforming the $(R\text{-}MBA)_2PbI_4$ counterparts of 0.14 and 0.088 A/W at 498 nm.

The specific detectivity D^* in the unit of Jones, which indicates the ability of a photodetector to detect low levels of incident power, can be calculated through eq 6:

$$D^* = \frac{R\sqrt{A}}{i_{noise}} \tag{6}$$

where R is the responsivity, A is the active area of the device, which is 0.05 cm^2 in this work, and i_{noise} is the noise current spectral density. Here, i_{noise} was calculated from the fast Fourier transform of the measured dark current versus time. The D^* and i_{noise} values are summarized in Table S3. Figure 3e shows that the 0.2 and 0.3 M $(R\text{-}MBA_{0.5}nBA_{0.5})_2PbI_4$ photodetectors exhibit D^* values with maxima of 2.45×10^{12} and 1.59×10^{12} Jones at 503 nm under 0 V bias, respectively, surpassing the $(R\text{-}MBA)_2PbI_4$ counterparts of 1.12×10^{12} and 1.46×10^{12} Jones at 498 nm. The highest D^* exhibited by the 0.2 M $(R\text{-}MBA_{0.5}nBA_{0.5})_2PbI_4$ photodetector could benefit from the preferred orientation of $(R\text{-}MBA_{0.5}nBA_{0.5})_2PbI_4$ perovskites, enhancing their out-of-plane charge transport while also realizing the low i_{noise}. The lowest D^* exhibited by the 0.2 M $(R\text{-}MBA)_2PbI_4$ photodetector is largely due to the high i_{noise}, which could be related to the relatively lower film quality shown in GIWAXS results (Figure S5a).

The response speeds of the chiral photodetectors were measured under unpolarized light at 500 nm (1.0 mW cm^{-2}) with 0 V bias. The responses of all of the chiral photodetectors show stable and reproducible current−time curves, as shown in Figure S11b. The rise time (τ_r) of the transient photocurrent corresponds to the duration in which the output signal increases from 10 to 90% of its saturated value, with saturation occurring as excitons reach equilibrium. Subsequently, upon switching off the illumination, the decay of the photocurrent is characterized by a fall time (τ_f). The values of τ_r and τ_f are summarized in Table S3. The photodetectors with thicker films show both slower τ_r and τ_f values compared to their thinner counterparts (Figure 3f), attributable to the increased diffusion distance in thicker films. Notably, the photodetectors with the similar thicknesses exhibit comparable τ_r, while the τ_f of the $(R\text{-}MBA_{0.5}nBA_{0.5})_2PbI_4$ photodetectors, particular the one with a thicker film, is faster than that of $(R\text{-}MBA)_2PbI_4$. This phenomenon can be contributed to the larger built-in potential of $(R\text{-}MBA_{0.5}nBA_{0.5})_2PbI_4$ under illumination, effectively promoting the separation and extraction of photogenerated electron−hole pairs,[45] leading to a faster fall time.

Given the optimal device performance exhibited by the chiral photodetectors based on 0.2 M $(R\text{-}MBA_{0.5}nBA_{0.5})_2PbI_4$ and 0.3 M $(R\text{-}MBA)_2PbI_4$ films, we also fabricated the chiral photodetectors based on 0.2 M $(S\text{-}MBA_{0.5}nBA_{0.5})_2PbI_4$ and 0.3 M $(S\text{-}MBA)_2PbI_4$ films. These devices exhibit similar values and features of $J-V$ curves, EQE, R, and D^* compared to their enantiomer counterparts (Figure S12a−e), indicating the photodetectors based on R- and S-chiral 2D perovskites performing no difference in detecting unpolarized light.

To assess the performance of these optimal chiral photodetectors in distinguishing the polarization states of RCP and LCP photons, we measured the photocurrent density of the devices under illumination of RCP and LCP light (Figure 4a). Based on the CD spectra, the monochromatic RCP and LCP lights at 510 and 505 nm (0.5 mW/cm^{-2}) were selected for 0.2 M $(R,S\text{-}MBA_{0.5}nBA_{0.5})_2PbI_4$ and 0.3 M $(R,S\text{-}MBA)_2PbI_4$, respectively. As shown in Figure 4b,c, the photodetectors based on 0.2 M $(R\text{-}MBA_{0.5}nBA_{0.5})_2PbI_4$ and 0.3 M $(R\text{-}MBA)_2PbI_4$ show higher photocurrent densities under RCP light illumination than those under LCP light illumination, while the photodetectors based on their enantiomer 0.2 M $(S\text{-}MBA_{0.5}nBA_{0.5})_2PbI_4$ and 0.3 M $(S\text{-}MBA)_2PbI_4$ show the reverse trend, demonstrating the selectivity of spin-polarized carrier transport. To quantify the capability of the devices in selectively detecting on handiness light over the other, we calculated the distinguishability of response to the LCP and RCP light (g_{res}) according to the following equation:

$$g_{res} = \frac{2(J_L - J_R)}{(J_L + J_R)} \tag{7}$$

https://doi.org/10.1021/acsnano.4c02588
ACS Nano 2024, 18, 14605−14616

where J_L and J_R represent the photocurrent density under LCP and RCP illumination, respectively. The g_{res} factor ranges from −2 to +2, which stands for pure RCP or LCP light detection, respectively, whereas 0 indicates no distinguishability between LCP and RCP light. At 0 V bias, the photodetectors based on 0.2 M $(R,S\text{-}MBA_{0.5}nBA_{0.5})_2PbI_4$ exhibit high g_{res} factors of −0.58 and +0.54, respectively (Figure 4b), surpassing the highest g_{res} reported for 2D perovskite CPL detectors based on a photodiode device architecture (Table 1 and Figure 4i). However, the g_{res} factors of the photodetectors based on 0.3 M $(R,S\text{-}MBA)_2PbI_4$ are −0.18 and +0.19, respectively (Figure 4c), about three times lower than the photodetector base on 0.2 M $(R,S\text{-}MBA_{0.5}nBA_{0.5})_2PbI_4$. We further applied external bias to enhance spin transport and consequently increase the photocurrent anisotropy. The $J-V$ curves of the photodetectors with 0.2 M $(R,S\text{-}MBA_{0.5}nBA_{0.5})_2PbI_4$ and 0.3 M $(R,S\text{-}MBA)_2PbI_4$ show stable g_{res} factors under the operating bias from 0 to −1 V (Figure 4d−g). The zoomed-in $J-V$ curves over the bias range of 0 to −1 V are shown in Figure S13. All of the chiral photodetectors exhibit an ∼10% higher value of g_{res} when a −1 V bias is applied (Figure 4h), which facilitates faster spin transport and highlights the excellent CPL detection ability of $(R,S\text{-}MBA_{0.5}nBA_{0.5})_2PbI_4$.

The increase in the thickness of the 0.3 M $(R\text{-}MBA_{0.5}nBA_{0.5})_2PbI_4$ film leads to a slight decrease in the g_{res} factor to −0.51 of the CPL response at 0 V bias (Figure S14a). This reduction can be attributed to the decreased difference between the carrier concentrations (Δc) generated by LCP and RCP light illumination in thicker films, consistent with the conclusion drawn from eq 2.[41] This reduced g_{res} factor of the 0.3 M $(R\text{-}MBA_{0.5}nBA_{0.5})_2PbI_4$ film can also be explained by the higher g_{CD} of thin 0.2 M $(R\text{-}MBA_{0.5}nBA_{0.5})_2PbI_4$ films compared to that of the thick 0.3 M $(R\text{-}MBA_{0.5}nBA_{0.5})_2PbI_4$ films. Moreover, the g_{res} of CPL response is 2 orders of magnitude larger than the g_{CD} of the chiral perovskite thin films, which is attributed to the spin-dependent carrier generation, transport, and collection for chiral perovskites under CPL excitation.[50] The non-optimal photodetector based on the 0.2 M $(R\text{-}MBA)_2PbI_4$ film shows a much lower g_{res} factor of −0.08 at 0 V bias (Figure S14b), which is due to the significant reduction in g_{CD} and inefficient carrier collection.

CONCLUSIONS

In summary, we fabricated chiral 2D perovskites with mixed aryl, chiral and alkyl, achiral organic cations and deployed them to the photodiode-type CPL photodetectors. The chiral 2D perovskite with the formula of $(R,S\text{-}MBA_{0.5}nBA_{0.5})_2PbI_4$ exhibits a g_{CD} of 2.89×10^{-3}, which is a 10-fold enhancement in chirality amplitude compared to the chiral 2D perovskite fabricated with pure aryl, chiral organic cations with the formula of $(R,S\text{-}MBA)_2PbI_4$. The photodiode-type CPL photodetectors fabricated with 0.2 M $(R,S\text{-}MBA_{0.5}nBA_{0.5})_2PbI_4$ (∼220 nm thick) exhibit high g_{res} factors of −0.58 and 0.54, respectively, surpassing the highest reported values for CPL detectors based on chiral 2D perovskites. Moreover, the fabricated CPL photodetectors show self-powered capability with a D^* of 2.45×10^{12} Jones at 0 V bias. This work demonstrates that mixing aryl, chiral cations with alkyl, achiral cations in 2D perovskites offers an effective way to amplify the chirality and makes it possible to develop CPL-selective photodetectors for potential applications in polarization-sensitive imaging systems, information encryption, and drug discovery.

METHODS

Chemical Materials. Lead(II) iodide (PbI_2, 99.99%), *N*,*N*-dimethylformamide (DMF, anhydrous, ≥ 99.8%), diethyl ether (≥99%), *N*,*N*-dimethyl sulfoxide (DMSO, anhydrous, ≥99.9%), ethanol (≥99.5%), chlorobenzene (CB, anhydrous, ≥99.8%), hydroiodic acid (57 wt % stabilized with 1.5% hypophosphorous acid), organic amine (±)-α-methylbenzylamine (rac-MBA, >98%), (R)-(+)-α-methylbenzylamine (R-MBA, >98%), (S)-(−)-α-methylbenzylamine (S-MBA, >98%), [6,6]-phenyl C61 butyric acid methyl ester (PCBM, >99.9%), and bathocuproine (BCP, 99.99%) were purchased from Sigma-Aldrich (St. Louis, Missouri). Butylammonium iodide (BAI) was purchased from GreatCell Solar (Queanbeyan, Australia). A poly(3,4-ethylenedioxythiophene)-poly(styrenesulfonate) (PEDOT:PSS) solution (Clevios P VP AI 4083) was purchased from Heraeus (Hanau, Germany). The SnO_2 nanoparticle (15% in H_2O colloidal dispersion) was purchased from Alfa Aesar (Haverhill, Massachusetts). Aluminum and silver pellets of 99.999% purity were purchased from R. D. Mathis (Long Beach, CA). All of the purchased chemicals were used without further purification.

(R)/(S)-MBAI Synthesis. (R)/(S)-MBAI was synthesized by dissolving (R)/(S)-MBA (5 mL) in 30 mL of ethanol in an ice bath. A hydroiodic acid aqueous solution (5.8 mL) was added dropwise to the flask with vigorous stirring. After the addition of hydroiodic acid, the mixture was allowed to stand in an ice bath for 1 h. The crude product was obtained by slowly evaporating the solvent under reduced pressure. The white precipitate was then redissolved in ethanol and recrystallized with diethyl ether. The small crystals were further washed with diethyl ether several times before being dried in a vacuum oven.

Chiral 2D Perovskite Thin Film Fabrication. Plain glass substrates (Fisher Scientific) were cut into 15 mm × 15 mm sizes and cleaned via ultrasonication for 15 min in detergent in soapy Millipore deionized water, Millipore deionized water, acetone, and isopropanol in sequence. The cleaned substrates were treated with oxygen plasma at 100 W for 10 min. The substrates were transferred to a N_2-filled glovebox to make chiral 2D perovskite films. To prepare the precursor, synthesized (R)/(S)-MBAI and *n*BAI were dissolved in DMF/DMSO along with PbI_2 at designated ratios to satisfy the chemical formulas of $(R,S\text{-}MBA)_2PbI_4$ and $(R,S\text{-}MBA_{0.5}nBA_{0.5})_2PbI_4$. Specifically, the mole ratio between the total amount of organic ammonium cations and the amount of PbI_2 was 2:1. Additionally, DMSO was added to the solutions, and the ratio of DMSO to lead cations was 1:1. Then, DMF was added to the solutions to make the Pb^{2+} concentration in the solutions to be 0.2 or 0.3 M. The resulting solutions were spin-coated onto a glass substrate at 1000 rpm for 10 s and 3000 rpm for 30 s. Chlorobenzene as an antisolvent was dripped during the spin coating process. The substrate was then heated at 100 °C for 10 min.

Chiral Photodetector Fabrication. Chiral photodetectors were fabricated with the configuration of ITO/PEDOT:PSS/chiral 2D perovskites/PCBM/BCP/Al. ITO-coated glass substrates were cleaned by the same methods as described above. The PEDOT:PSS solution was filtered through a 0.45 μm nylon syringe filter and spin-coated onto a cleaned ITO/glass substrate at 5000 rpm for 40 s, followed by annealing at 150 °C for 20 min. The chiral 2D perovskite layer was fabricated as described above. A 20 mg/mL PCBM in chlorobenzene solution and a 0.5 mg/mL BCP in isopropanol solution were prepared. The substrates were respectively spin-coated with PCBM at 1000 rpm for 40 s and BCP at 4000 rpm for 40 s. The devices were completed by depositing a 100 nm Al layer onto their surfaces through a shadow mask, defining an active area of 0.05 cm^2.

Electron-Only and Hole-Only Device Fabrication. Electron-only photodetectors were fabricated with a configuration of ITO/SnO_2/chiral 2D perovskites/PCB/Ag. ITO-coated glass substrates were cleaned by the same methods described above. A SnO_2 layer was coated by spin-coating a diluted aqueous solution of 2.5 wt % SnO_2 nanoparticles onto a cleaned ITO/glass substrate at 3000 rpm for 30 s, followed by annealing at 150 °C for 30 min. The chiral 2D perovskite and PCBM layer were fabricated as described above. The

https://doi.org/10.1021/acsnano.4c02588
ACS Nano 2024, 18, 14605−14616

devices were completed by depositing a 100 nm Ag layer onto their surfaces through a shadow mask, defining an active area of 0.05 cm^2. Hole-only photodetectors were fabricated with a configuration of ITO/PEDOT:PSS/chiral 2D perovskites/MoO_3/Ag. ITO-coated glass substrates were cleaned by the same methods described above. The PEDOT:PSS and chiral 2D perovskite layers were fabricated as described above. These devices were completed by depositing a 10 nm MoO_3 layer followed by a 100 nm Ag layer onto their surfaces through a shadow mask, defining an active area of 0.05 cm^2.

Thin Film Characterization. Ultraviolet−visible (UV−vis) absorption spectra were collected by using a Varian Cary 5000 UV−vis−NIR spectrophotometer. Steady-state photoluminescence (PL) measurements of the thin films were captured by using an Edinburgh FLS1000 spectrometer with an excitation wavelength of 400 nm. The transmission circular dichroism (CD) data of the thin films were collected by using a CD spectrometer (J-1500, JASCO). Two-dimensional X-ray diffraction (XRD) patterns were collected with a Rigaku SmartLab X-ray diffractometer using Cu Kα radiation (λ = 1.5405 Å). The grazing-incidence wide-angle X-ray scattering (GIWAXS) measurements were conducted at the Complex Materials Scattering (CMS, 11-BM) beamline of National Synchrotron Light Source II (NSLS-II) at the Brookhaven National Laboratory. The X-ray beam has a size of 200 μm (horizontally) × 50 μm (vertically), a divergence of 1 mrad, and an energy of 13.5 keV with a resolution of 0.7%. The perovskite films were deposited on 1.5 cm × 1.5 cm ITO glass and were measured with an exposure time of 5 s at incidence angles of 0.20° with respect to the substrate plane. The scattered data were collected with a customized Pilatus 800K area detector (Dectris, Switzerland), which consists of 0.172 mm square pixels in a 1043 × 981 array, placed 0.260 m downstream with respect to the sample position. The collected 2D-scattering patterns were visualized and analyzed by a custom Python script developed by the authors. Scanning electron microscopy (SEM) images were acquired using an FEI Sirion SEM operated at 3 kV to analyze surface morphology.

Chiral Photodetector Characterization. Unpolarized light was then converted to CPL by using a quarter-wave plate (Thorlabs, AQWP05M-580) and two linear polarizers (Thorlabs, LPVISA050). $J-V$ curves, EQE, and response speed in the dark and under unpolarized illumination and circular polarized illumination were measured with a QE-RX system (EnliTech).

ASSOCIATED CONTENT

Supporting Information

The Supporting Information is available free of charge at https://pubs.acs.org/doi/10.1021/acsnano.4c02588.

Chiroptical and structural properties of the 0.2 and 0.3 M $(R,S\text{-MBA})_2PbI_4$ and $(R,S\text{-MBA}_{0.5}nBA_{0.5})_2PbI_4$ films; energy diagram of the chiral photodetector, electron-only, and hole-only devices; illustrations of the charge injection, generation, and transport in a device; SCLC measurements, carrier charge mobility, and carrier trap density based on the electron-only and hole-only devices; $J-V$ curves, EQE, responsivity, specific detectivity, and response speed spectra of the photodetectors under unpolarized light based on 0.3 M $(S\text{-MBA})_2PbI_4$ and 0.2 M $(S\text{-MBA}_{0.5}nBA_{0.5})_2PbI_4$; $J-V$ curves under RCP and LCP light illumination of the photodetectors with the 0.2 M $(R,S\text{-MBA}_{0.5}nBA_{0.5})_2PbI_4$ and 0.3 M $(R,S\text{-MBA})_2PbI_4$ films (PDF)

AUTHOR INFORMATION

Corresponding Author

Qiuming Yu − *Robert Frederick Smith School of Chemical and Biomolecular Engineering, Cornell University, Ithaca, New York 14853, United States;* orcid.org/0000-0002-2401-4664; Email: qy10@cornell.edu

Authors

Xiaoyu Zhang − *Robert Frederick Smith School of Chemical and Biomolecular Engineering, Cornell University, Ithaca, New York 14853, United States;* orcid.org/0000-0002-6010-1108

Yuanze Xu − *Robert Frederick Smith School of Chemical and Biomolecular Engineering, Cornell University, Ithaca, New York 14853, United States;* orcid.org/0000-0002-4873-6629

Anna Niamh Alphenaar − *Department of Chemistry and Chemical Biology, Cornell University, Ithaca, New York 14853, United States*

Shripathi Ramakrishnan − *Robert Frederick Smith School of Chemical and Biomolecular Engineering, Cornell University, Ithaca, New York 14853, United States*

Yugang Zhang − *Center for Functional Nanomaterials, Brookhaven National Laboratory, Upton, New York 11973, United States*

Adewale Joseph Babatunde − *Robert Frederick Smith School of Chemical and Biomolecular Engineering, Cornell University, Ithaca, New York 14853, United States*

Complete contact information is available at: https://pubs.acs.org/10.1021/acsnano.4c02588

Notes

The authors declare no competing financial interest.

ACKNOWLEDGMENTS

This work was financially supported by the National Science Foundation (NSF) (nos. EPM-2114350 and EPMD-2054942). This work made use of the Cornell Center for Materials Research Shared Facilities, which is supported through the NSF MRSEC program (no. DMR-1719875) and GIWAXS from the CMS beamline (11-BM) of National Synchrotron Light Source II, supported by the U.S. DOE Office of Science Facilities at Brookhaven National Laboratory under contract no. DE-SC0012704.

REFERENCES

(1) El-Hassan, M. A; Farahat, A. E.; Hussein, K. F. Circularly Polarized 28 GHz Compact Patch Antenna for 5G Mobile Communications. In *2021 International Telecommunications Conference (ITC-Egypt)*; IEEE: 2021; pp 1−6.

(2) Ren, J.-G.; Xu, P.; Yong, H.-L.; Zhang, L.; Liao, S.-K.; Yin, J.; Liu, W.-Y.; Cai, W.-Q.; Yang, M.; Li, L.; Yang, K.-X.; Han, X.; Yao, Y.-Q.; Li, J.; Wu, H.-Y.; Wan, S.; Liu, L.; Liu, D.-Q.; Kuang, Y.-W.; He, Z.-P.; et al. Ground-to-Satellite Quantum Teleportation. *Nature* **2017**, *549*, 70−73.

(3) Sherson, J. F.; Krauter, H.; Olsson, R. K.; Julsgaard, B.; Hammerer, K.; Cirac, I.; Polzik, E. S. Quantum Teleportation between Light and Matter. *Nature* **2006**, *443*, 557−560.

(4) Yao, Q.; Bie, Y.-Q.; Chen, J.; Li, J.; Li, F.; Cao, Z. Anapole Enhanced On-Chip Routing of Spin−Valley Photons in 2D Materials for Silicon Integrated Optical Communication. *Opt. Lett.* **2021**, *46*, 4080−4083.

(5) Silvestri, I. P.; Colbon, P. J. J. The Growing Importance of Chirality in 3D Chemical Space Exploration and Modern Drug Discovery Approaches for Hit-ID. *ACS Med. Chem. Lett.* **2021**, *12*, 1220−1229.

(6) MacKenzie, L. E.; Pal, R. Circularly Polarized Lanthanide Luminescence for Advanced Security Inks. *Nat. Rev. Chem.* **2021**, *5*, 109−124.

(7) Sun, Z.; Huang, Y.; Bao, Y.; Wu, D. Polarized Remote Sensing: A Note on the Stokes Parameters Measurements from Natural and

Man-Made Targets Using a Spectrometer. *IEEE Trans. Geosci. Remote Sens.* **2017**, *55*, 4008−4021.
(8) Long, G.; Sabatini, R.; Saidaminov, M. I.; Lakhwani, G.; Rasmita, A.; Liu, X.; Sargent, E. H.; Gao, W. Chiral-Perovskite Optoelectronics. *Nat. Rev. Mater.* **2020**, *5*, 423−439.
(9) Lu, H.; Vardeny, Z. V.; Beard, M. C. Control of Light, Spin and Charge with Chiral Metal Halide Semiconductors. *Nat. Rev. Chem.* **2022**, *6*, 470−485.
(10) Duan, T.; Zhou, Y. Leveraging Hierarchical Chirality in Perovskite(-Inspired) Halides for Transformative Device Applications. *Adv. Energy Mater.* **2023**, *13*, 2200792.
(11) Ma, J.; Wang, H.; Li, D. Recent Progress of Chiral Perovskites: Materials, Synthesis, and Properties. *Adv. Mater.* **2021**, *33*, 2008785.
(12) Jana, M. K.; Song, R.; Liu, H.; Khanal, D. R.; Janke, S. M.; Zhao, R.; Liu, C.; Valy Vardeny, Z.; Blum, V.; Mitzi, D. B. Organic-to-Inorganic Structural Chirality Transfer in a 2D Hybrid Perovskite and Impact on Rashba-Dresselhaus Spin-Orbit Coupling. *Nat. Commun.* **2020**, *11*, 4699.
(13) Son, J.; Ma, S.; Jung, Y. K.; Tan, J.; Jang, G.; Lee, H.; Lee, C. U.; Lee, J.; Moon, S.; Jeong, W.; Walsh, A.; Moon, J. Unraveling Chirality Transfer Mechanism by Structural Isomer-Derived Hydrogen Bonding Interaction in 2D Chiral Perovskite. *Nat. Commun.* **2023**, *14*, 3124.
(14) Ahn, J.; Lee, E.; Tan, J.; Yang, W.; Kim, B.; Moon, J. A New Class of Chiral Semiconductors: Chiral-Organic-Molecule-Incorporating Organic−Inorganic Hybrid Perovskites. *Mater. Horiz.* **2017**, *4*, 851−856.
(15) Ahn, J.; Ma, S.; Kim, J.-Y.; Kyhm, J.; Yang, W.; Lim, J. A.; Kotov, N. A.; Moon, J. Chiral 2D Organic Inorganic Hybrid Perovskite with Circular Dichroism Tunable Over Wide Wavelength Range. *J. Am. Chem. Soc.* **2020**, *142*, 4206−4212.
(16) Lu, H.; Wang, J.; Xiao, C.; Pan, X.; Chen, X.; Brunecky, R.; Berry, J. J.; Zhu, K.; Beard, M. C.; Vardeny, Z. V. Spin-Dependent Charge Transport through 2D Chiral Hybrid Lead-Iodide Perovskites. *Sci. Adv.* **2019**, *5*, No. eaay0571.
(17) Lin, J.-T.; Chen, D.-G.; Yang, L.-S.; Lin, T.-C.; Liu, Y.-H.; Chao, Y.-C.; Chou, P.-T.; Chiu, C.-W. Tuning the Circular Dichroism and Circular Polarized Luminescence Intensities of Chiral 2D Hybrid Organic−Inorganic Perovskites through Halogenation of the Organic Ions. *Angew. Chem., Int. Ed.* **2021**, *60*, 21434−21440.
(18) Wang, J.; Fang, C.; Ma, J.; Wang, S.; Jin, L.; Li, W.; Li, D. Aqueous Synthesis of Low-Dimensional Lead Halide Perovskites for Room-Temperature Circularly Polarized Light Emission and Detection. *ACS Nano* **2019**, *13*, 9473−9481.
(19) Zhao, Y.; Qiu, Y.; Feng, J.; Zhao, J.; Chen, G.; Gao, H.; Zhao, Y.; Jiang, L.; Wu, Y. Chiral 2D-Perovskite Nanowires for Stokes Photodetectors. *J. Am. Chem. Soc.* **2021**, *143*, 8437−8445.
(20) Liu, Z.; Zhang, C.; Liu, X.; Ren, A.; Zhou, Z.; Qiao, C.; Guan, Y.; Fan, Y.; Hu, F.; Zhao, Y. S. Chiral Hybrid Perovskite Single-Crystal Nanowire Arrays for High-Performance Circularly Polarized Light Detection. *Adv. Sci.* **2021**, *8*, 2102065.
(21) Ma, J.; Fang, C.; Chen, C.; Jin, L.; Wang, J.; Wang, S.; Tang, J.; Li, D. Chiral 2D Perovskites with a High Degree of Circularly Polarized Photoluminescence. *ACS Nano* **2019**, *13*, 3659−3665.
(22) Sun, B.; Liu, X.-F.; Li, X.-Y.; Zhang, Y.; Shao, X.; Yang, D.; Zhang, H.-L. Two-Dimensional Perovskite Chiral Ferromagnets. *Chem. Mater.* **2020**, *32*, 8914−8920.
(23) Yuan, C.; Li, X.; Semin, S.; Feng, Y.; Rasing, T.; Xu, J. Chiral Lead Halide Perovskite Nanowires for Second-Order Nonlinear Optics. *Nano Lett.* **2018**, *18*, 5411−5417.
(24) Ishii, A.; Miyasaka, T. Direct Detection of Circular Polarized Light in Helical 1D Perovskite-Based Photodiode. *Sci. Adv.* **2020**, *6*, No. eabd3274.
(25) Yan, L.; Jana, M. K.; Sercel, P. C.; Mitzi, D. B.; You, W. Alkyl−Aryl Cation Mixing in Chiral 2D Perovskites. *J. Am. Chem. Soc.* **2021**, *143*, 18114−18120.
(26) Lee, C. U.; Ma, S.; Ahn, J.; Kyhm, J.; Tan, J.; Lee, H.; Jang, G.; Park, Y. S.; Yun, J.; Lee, J.; Son, J.; Park, J.-S.; Moon, J. Tailoring the Time-Averaged Structure for Polarization-Sensitive Chiral Perovskites. *J. Am. Chem. Soc.* **2022**, *144*, 16020−16033.
(27) Zhu, T.; Weng, W.; Ji, C.; Zhang, X.; Ye, H.; Yao, Y.; Li, X.; Li, J.; Lin, W.; Luo, J. Chain-to-Layer Dimensionality Engineering of Chiral Hybrid Perovskites to Realize Passive Highly Circular-Polarization-Sensitive Photodetection. *J. Am. Chem. Soc.* **2022**, *144*, 18062−18068.
(28) Ward, M. D.; Shi, W.; Gasparini, N.; Nelson, J.; Wade, J.; Fuchter, M. J. Best Practices in the Measurement of Circularly Polarised Photodetectors. *J. Mater. Chem. C* **2022**, *10*, 10452−10463.
(29) Wang, J.; Lu, H.; Pan, X.; Xu, J.; Liu, H.; Liu, X.; Khanal, D. R.; Toney, M. F.; Beard, M. C.; Vardeny, Z. V. Spin-Dependent Photovoltaic and Photogalvanic Responses of Optoelectronic Devices Based on Chiral Two-Dimensional Hybrid Organic−Inorganic Perovskites. *ACS Nano* **2021**, *15*, 588−595.
(30) Yao, B.; Wei, Q.; Yang, Y.; Zhou, W.; Jiang, X.; Wang, H.; Ma, M.; Yu, D.; Yang, Y.; Ning, Z. Symmetry-Broken 2D Lead−Tin Mixed Chiral Perovskite for High Asymmetry Factor Circularly Polarized Light Detection. *Nano Lett.* **2023**, *23*, 1938−1945.
(31) Li, X.; Hoffman, J. M.; Kanatzidis, M. G. The 2D Halide Perovskite Rulebook: How the Spacer Influences Everything from the Structure to Optoelectronic Device Efficiency. *Chem. Rev.* **2021**, *121*, 2230−2291.
(32) Umebayashi, T.; Asai, K.; Kondo, T.; Nakao, A. Electronic Structures of Lead Iodide Based Low-Dimensional Crystals. *Phys. Rev. B* **2003**, *67*, No. 155405.
(33) Even, J.; Pedesseau, L.; Dupertuis, M.-A.; Jancu, J.-M.; Katan, C. Electronic Model for Self-Assembled Hybrid Organic/Perovskite Semiconductors: Reverse Band Edge Electronic States Ordering and Spin-Orbit Coupling. *Phys. Rev. B* **2012**, *86*, No. 205301.
(34) Laur, P. The First Decades after the Discovery of CD and ORD by Aimé Cotton in 1895. In *Comprehensive Chiroptical Spectroscopy*; Berova, N.; Polavarapu, P. L.; Nakanishi, K.; Woody, R. W., Eds.; John Wiley & Sons, Ltd: 2012; pp 1−35.
(35) Salij, A.; Goldsmith, R. H.; Tempelaar, R. Theory of Apparent Circular Dichroism Reveals the Origin of Inverted and Noninverted Chiroptical Response under Sample Flipping. *J. Am. Chem. Soc.* **2021**, *143*, 21519−21531.
(36) Zhang, Z.; Wang, Z.; Sung, H. H.-Y.; Williams, I. D.; Yu, Z.-G.; Lu, H. Revealing the Intrinsic Chiroptical Activity in Chiral Metal-Halide Semiconductors. *J. Am. Chem. Soc.* **2022**, *144*, 22242−22250.
(37) Albano, G.; Pescitelli, G.; Di Bari, L. Chiroptical Properties in Thin Films of π-Conjugated Systems. *Chem. Rev.* **2020**, *120*, 10145−10243.
(38) Nordén, B.; Rodger, A.; Dafforn, T. Chapter 2 Spectroscopic Practicalities. In *Linear Dichroism and Circular Dichroism*; Nordén, B.; Rodger, A.; Dafforn, T., Eds.; The Royal Society of Chemistry: 2010; pp 15−48.
(39) Birkholz, M. Grazing Incidence Configurations. In *Thin Film Analysis by X-Ray Scattering*; John Wiley & Sons, Ltd: 2005; pp 143−182.
(40) Zheng, G.; Zhu, C.; Ma, J.; Zhang, X.; Tang, G.; Li, R.; Chen, Y.; Li, L.; Hu, J.; Hong, J.; Chen, Q.; Gao, X.; Zhou, H. Manipulation of Facet Orientation in Hybrid Perovskite Polycrystalline Films by Cation Cascade. *Nat. Commun.* **2018**, *9*, 2793.
(41) Chen, C.; Gao, L.; Gao, W.; Ge, C.; Du, X.; Li, Z.; Yang, Y.; Niu, G.; Tang, J. Circularly Polarized Light Detection Using Chiral Hybrid Perovskite. *Nat. Commun.* **2019**, *10*, 1927.
(42) He, T.; Li, S.; Jiang, Y.; Qin, C.; Cui, M.; Qiao, L.; Xu, H.; Yang, J.; Long, R.; Wang, H.; Yuan, M. Reduced-Dimensional Perovskite Photovoltaics with Homogeneous Energy Landscape. *Nat. Commun.* **2020**, *11*, 1672.
(43) Gao, Y.; Shi, E.; Deng, S.; Shiring, S. B.; Snaider, J. M.; Liang, C.; Yuan, B.; Song, R.; Janke, S. M.; Liebman-Peláez, A.; Yoo, P.; Zeller, M.; Boudouris, B. W.; Liao, P.; Zhu, C.; Blum, V.; Yu, Y.; Savoie, B. M.; Huang, L.; Dou, L. Molecular Engineering of Organic−Inorganic Hybrid Perovskites Quantum Wells. *Nat. Chem.* **2019**, *11*, 1151−1157.

https://doi.org/10.1021/acsnano.4c02588
ACS Nano 2024, 18, 14605−14616

(44) Seitz, M.; Magdaleno, A. J.; Alcázar-Cano, N.; Meléndez, M.; Lubbers, T. J.; Walraven, S. W.; Pakdel, S.; Prada, E.; Delgado-Buscalioni, R.; Prins, F. Exciton Diffusion in Two-Dimensional Metal-Halide Perovskites. *Nat. Commun.* **2020**, *11*, 2035.
(45) Su, L.; Yang, W.; Cai, J.; Chen, H.; Fang, X. Self-Powered Ultraviolet Photodetectors Driven by Built-In Electric Field. *Small* **2017**, *13*, 1701687.
(46) Lampert, M. A. Simplified Theory of Space-Charge-Limited Currents in an Insulator with Traps. *Phys. Rev.* **1956**, *103*, 1648−1656.
(47) Chen, J.; Kim, S.-G.; Park, N.-G. FA0.88Cs0.12PbI3−x(PF6)x Interlayer Formed by Ion Exchange Reaction between Perovskite and Hole Transporting Layer for Improving Photovoltaic Performance and Stability. *Adv. Mater.* **2018**, *30*, 1801948.
(48) Bube, R. H. Trap Density Determination by Space-Charge-Limited Currents. *J. Appl. Phys.* **1962**, *33*, 1733−1737.
(49) Muljarov, E. A.; Tikhodeev, S. G.; Gippius, N. A.; Ishihara, T. Excitons in Self-Organized Semiconductor/Insulator Superlattices: PbI-Based Perovskite Compounds. *Phys. Rev. B* **1995**, *51*, 14370−14378.
(50) Odenthal, P.; Talmadge, W.; Gundlach, N.; Wang, R.; Zhang, C.; Sun, D.; Yu, Z.-G.; Valy Vardeny, Z.; Li, Y. S. Spin-Polarized Exciton Quantum Beating in Hybrid Organic−Inorganic Perovskites. *Nat. Phys.* **2017**, *13*, 894−899.

https://doi.org/10.1021/acsnano.4c02588
ACS Nano 2024, 18, 14605−14616